Supplementary Information for Monofiber-Based Temperature and Strain Discrimination using Heterogeneous Waveguide Bragg Gratings

Junxian Luo[1], Hanwen Liu[2], Haotian Ding[2], Zhengda Zhang[2], Zhuo Chen[1], Fei Xu[2, *]

[1] School of Physics, Nanjing University, Nanjing, 210023, Jiangsu Province, China

[2] College of Engineering and Applied Sciences, Nanjing University, Nanjing, 210023, Jiangsu Province, China

*feixu@nju.edu.cn

S1: Waveguide fabrication

According to the principles of coupled-mode theory (CMT) governing optical waveguides[1], the inter-waveguide coupling coefficient (κ) critically influences the efficiency of evanescent field coupling. Coupling coefficient is intrinsically linked to the refractive index (RI) profile and the mode field overlap integral between fiber core and cladding waveguide. In this study, a multiple move scanning fabrication approach was employed, where iterative writing cycles near the optical fiber core induced progressive modifications to the RI distribution. Notably, stress accumulation exhibited pronounced enhancement with successive inscribed cycles[2]. Owing to the complexity of precisely characterizing the RI profile under these conditions, the optimal number of required inscribe cycles was determined experimentally.

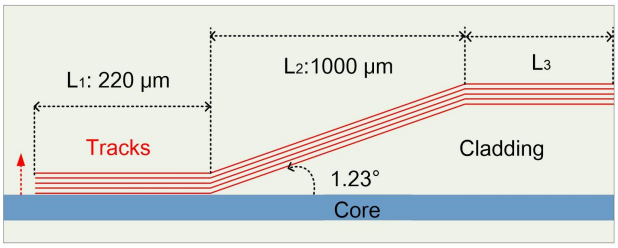

Figure S1. Schematic of cladding waveguide inscribed by multiple move scanning method.

The experimental methodology involved maintaining a fixed coupling length while incrementally inscribed multiple waveguide tracks. As illustrated in Figure S1 the inscription initiated at a distance of 5 μm from the single mode fibe (SMF) core center, with sequential tracks laterally offset by 500 nm increments to decouple light from the core. Key geometric parameters included a primary coupling length L_1 = 220 μm, a deflection angle of 1.23° within the deflection length L_2 = 1000 μm, and terminal waveguide positioning exceeding 20 μm from the core to ensure complete decoupling.

The optical intensity of 1550 nm wavelength light transmitted in the SMF

with inscribed cladding waveguides was monitored. Under non-inscribed conditions, the power meter exhibited a baseline reading of 0 dB. A sequential inscription was implemented wherein 9 times tracks were performed, with optical power measurements recorded following each inscription. Five independent samples test data presented in Figure S2. The black point in Figure S2 represents mean insertion loss, while error bars indicate standard deviation of five samples. After 7 times tracks inscribed, the average transmission loss is 2.78 ± 0.48 dB, corresponds to 47.3% optical power was decoupled from the fiber core. The nearly 1:1 waveguide splitting ratio makes it suitable for the further fabrication of sensors. Therefore, the waveguide inscribed by the 7 times stracks was used to fabricate sensors.

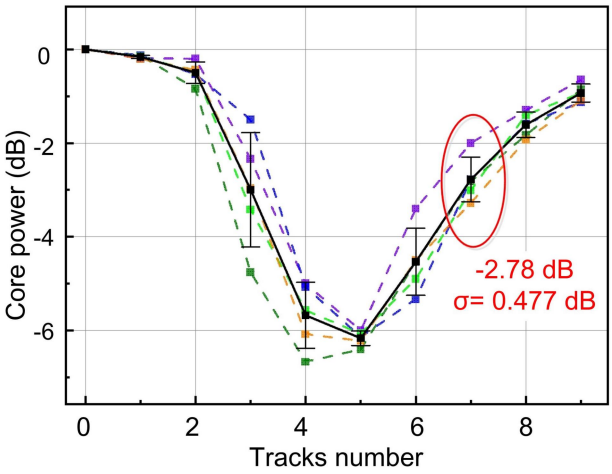

Figure S2. The relationship between the number of tracks of the cladding waveguide and the decoupling energy from SMF core.

As shown in Figure S3(a), through 7 times tracks scanning passes, a waveguide with a width of ~5 μm was fabricated in the SMF cladding. Subsequent axial rotation of the optical fiber by 90°, as depicted in Figure S3(b), revealed distinct RI modulation. The upper region exhibits a negative RI modulation, while localized material compression occurs, generating a lower region with a positive RI modulation of ~8 μm in depth, closely matching the core diameter of SMF.

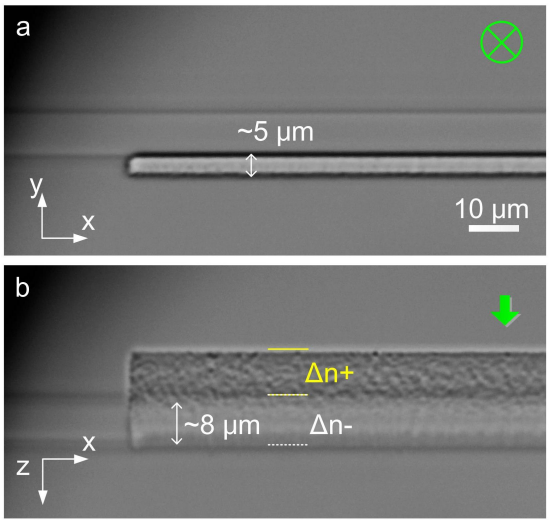

Figure S3. Microscopic images of cladding waveguides. a, Top view. **b,** Top view of the SMF after rotating 90° along the axial direction.

S2: RI distribution of the waveguides

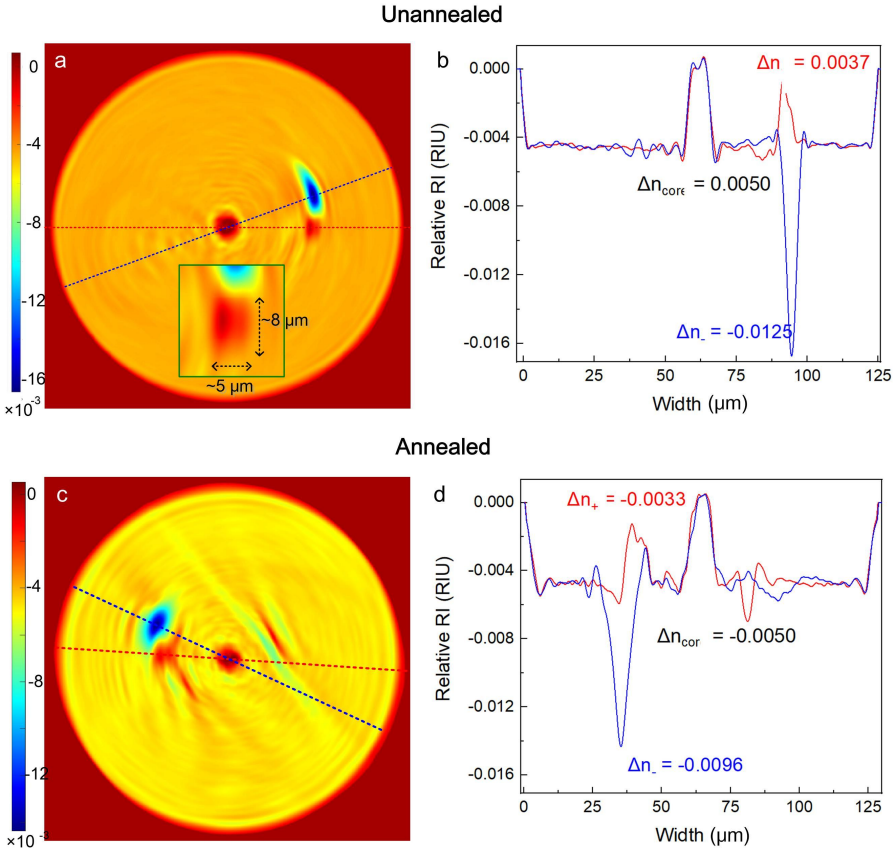

Figure S4. RI distribution of the SMF cladding waveguide before and after annealing. a, 2D distribution map of the cladding waveguide's RI before annealing. **b,** RI profile line of (a). **c,** 2D distribution map of the cladding waveguide's RI after annealing. **d,** RI profile line of (c).

The waveguides fabricated within the SMF cladding, with characterization of its RI distribution. As shown in Figure S4(a), the positive RI modulation region (highlighted in the green inset) exhibits approximate horizontal and vertical dimensions of 5×8 μm. The RI profiles were extracted along the red and blue dotted lines in Figure S4(a) and plotted in Figure S4(b). The maximum positive RI modulation (Δn = +0.0037 RIU), corresponding to the red profile, was marginally lower than the core-cladding refractive index contrast (Δn = +0.005 RIU); the blue profile demonstrates a negative modulation (Δn = -0.0125 RIU). Additionally, since the waveguide was written from right to left, the stress accumulation on the left side of the waveguide is the greatest, resulting in uneven RI modulation.

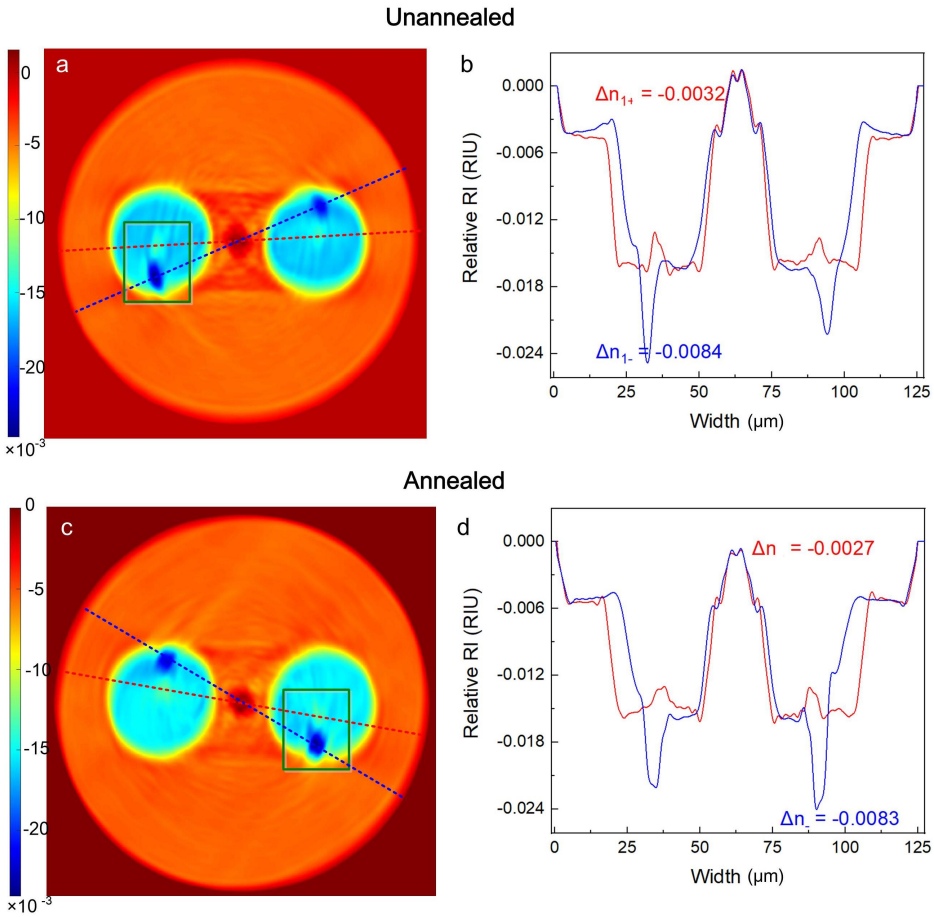

Figure S5. RI distribution of the SRW before and after annealing. a, 2D distribution map of the SRW's RI before annealing. **b,** RI profile line of (a). **c,** 2D distribution map of the SRW's RI after annealing. **d,** RI profile line of (c).

Another waveguide fabricated with the same parameters was subjected to 24 hour of 290 °C annealing. Its RI distribution and profiles is shown in Figure S4(c) and (d). The maximum positive and negative RI modulations of this waveguide decreased to +0.0033 RIU and -0.0096 RIU, respectively. The RI modulation reduction caused by annealing changed the coupling coefficient of the waveguide, resulting in the intensity changes of the SRW grating and CW grating as shown in Figure 2(a).

The stress rod waveguides (SRW) fabricated within the polarization-maintaining fiber (PMF) stress rod. Its RI distribution and profiles is shown in Figure S5(a) and (b). The maximum positive and negative RI modulations of the SRW are +0.0032 RIU and -0.0084 RIU, respectively. Another SRWs sample fabricated with the same parameters was subjected to 24 hour of 290°C annealing. The maximum positive and negative RI modulations of the SRW decreased to +0.0027 RIU and -0.0083 RIU, respectively. The reduction of the effective RI of the SRW and the partial stress release led to blue shifts of the gratings' resonant wavelength after cooling.

S3: Comparison of sensors' performance

Table S1 summarizes previous studies about temperature and strain discrimination based on fiber Bragg grating (FBG). The strain measurement accuracy of the devices under static or dynamic temperature changes was compared. Under static thermal conditions, the temperature compensators demonstrate relatively lax requirement with spatial proximity and measurement points. Conversely, dynamic thermal conditions need higher compensation density. For example, as proposed in the research of Ref. [10], 10 temperature compensators need to be installed to achieve better strain measurement accuracy. By contrast, the proposed monofiber sensor in this article exhibits higher strain measurement accuracy and more compact size under dynamic temperature changes .

Table S1 Comparison of Sensors' Performances

Sensor or system	Strain measurement accuracy (με)	measurement state	Ref.
polarization-maintaining FBG	~20	Static	3
Cascaded FBG with different packages	±40	Static	4
Parallel whispering gallery mode cavity and FBG	±36	Static	5
FBG with laser direct writing sawtooth stressor	28	Static	6
Few-mode FBG	20.04	Static	7
FBG with isolated compensation	207.2	Static	8
Cascaded FBG with different packages	89.1	Dynamic	9
FBGs with 10 temperature compensators	55	Dynamic	10
This work	~±20	Dynamic	★

References

1. Yariv, A. Coupled-mode theory for guided-wave optics. *IEEE Journal of Quantum Electronics* **9**, 919-933 (2003).
2. Lee, T. et al. Low bend loss femtosecond laser written waveguides exploiting integrated microcrack. *Scientific Reports* **11**, 23770 (2021).
3. Zhu, M. et al. Dependence of measurement accuracy on the birefringence of PANDA fiber Bragg gratings in distributed simultaneous strain and temperature sensing. *Optics Express* **25**, 4000-4017 (2017).
4. Shiratsuchi, T. & Imai, T. Development of fiber Bragg grating strain sensor with temperature compensation for measurement of cryogenic structures. *Cryogenics* **113**, 103233 (2021).
5. Lee, A., Lee, S.-K. & Lee, S.H. Simultaneous temperature and strain sensing with hybrid resonator of fiber Bragg grating and whispering gallery resonator. *IEEE Sensors Journal* **20**, 2962-2966 (2019).
6. Guo, K. et al. Simultaneous measurement of strain and temperature by a sawtooth stressor-assisted highly birefringent fiber Bragg grating. *Journal of Lightwave Technology* **38**, 2060-2066 (2020).

7. Hao, Y. et al. Error Analysis and Experimental Research of Temperature/Strain Sensing Based on Few-Mode Fiber Bragg Grating. *Fiber and Integrated Optics* **43**, 219-233 (2024).
8. Guinchard, M. et al. in 9th International Particle Accelerator Conference 2572-2574 (2018).
9. Yao, K. et al. Design and analysis of a combined FBG sensor for the measurement of three parameters. *IEEE Transactions on Instrumentation and Measurement* **70**, 1-10 (2021).
10. Liang, Z. et al. FBG-based strain monitoring and temperature compensation for composite tank. *Aerospace Science and Technology* **127**, 107724 (2022).